Transition of the Reaction from Three-Phase to Two-Phase by Using a Hybrid Conductor for High-Energy-Density High-Rate Solid-State Li-O₂ Batteries

Changtai Zhao[+], Yuanmin Zhu[+], Qian Sun, Changhong Wang, Jing Luo, Xiaoting Lin, Xiaofei Yang, Yang Zhao, Ruying Li, Shangqian Zhao, Huan Huang, Li Zhang, Shigang Lu, Meng Gu,* and Xueliang Sun*

Abstract: *Solid-state Li-O₂ batteries possess the ability to deliver high energy density with enhanced safety. However, designing a highly functional solid-state air electrode is the main bottleneck for its further development. Herein, we adopt a hybrid electronic and ionic conductor to build solid-state air electrode that makes the transition of Li-O₂ battery electrochemical mechanism from a three-phase process to a two-phase process. The solid-state Li-O₂ battery with this hybrid conductor solid-state air electrode shows decreased interfacial resistance and enhanced reaction kinetics. The Coulombic efficiency of Li-O₂ battery is also significantly improved, benefiting from the good contact between discharge products and electrode materials. In situ environmental transmission electron microscopy under oxygen was used to illustrate the reversible deposition and decomposition of discharge products on the surface of this hybrid conductor, visually verifying the two-phase reaction.*

The Li-O₂ battery is a promising rechargeable battery candidate owing to its ultrahigh theoretical energy density.[1] However, safety concerns and poor cycling stability of Li-O₂ batteries originating from the formation of Li dendrites and use of organic liquid electrolytes (LEs) inhibit their practical applications.[2] Therefore, the development of solid-state Li-O₂ battery is a promising direction to suppress the Li

dendrites growth, avoid the evaporation and leakage of organic LEs, and prevent the Li metal anode from corrosion by air.[3] However, the lack of successful design of solid-state air electrodes has long limited the development of solid-state Li-O₂ batteries.[4]

In general, there are multiple performance-determining solid-state interfaces in a solid air electrode. The flowing air and discharge products (Li₂O and Li₂O₂) must be interfaced with the electronic conductors and ionic conductors to ensure complete electrochemical cycling.[5] In most cases for solid-state electrodes, these essential interfaces are distributed discontinuously and in the form of point-to-point. As a result, the large interfacial resistance leads to high discharge/charge polarization and quick failure.[6] More specifically, solid-state Li-O₂ batteries experience high overpotential, low specific capacity, poor rate performance, and short cycle lives.[7] To alleviate the problems, Zhou's group reported a solar-driven strategy to efficiently accelerate the oxidation of Li₂O₂ and reduce the overpotential of solid-state Li-O₂ batteries.[8] For further advancement of solid-state Li-O₂ batteries, demonstration of rational and optimized air electrode design is an important step. Minimizing the number of interfaces and distributing the essential ionic/electronic contacts evenly are potential approaches.

Herein, we report on a novel strategy of using a hybrid ionic and electronic conductor to optimize the interface for transporting Li ions and electrons and to enhance the performance of solid-state Li-O₂ batteries. In the hybrid material, the core of nitrogen-doped carbon nanotube (NCNT) as the electronic conductor is responsible for electron transfer, while the coating layer of LiTaO₃ as the ionic conductor is used for Li-ion conduction. As a result, the facet-to-facet interface overcomes the interface of point-to-point limitations and significantly enhances the electroactive area of the electrode. The discharge products can be smoothly deposited and decomposed on the hybrid conductor surface upon charge and discharge. The significantly decreased interfacial resistance of the battery, improved reaction kinetics, and enhanced Coulombic efficiency also evidence the effectiveness of this approach. To visualize the electrochemical effect of the hybrid conductor, a solid-state Li-O₂ nanobattery is configured for real-time in situ imaging of the structural and compositional evolution during oxygen reduction reaction (ORR) and oxygen evolution reaction (OER) processes. Uniform deposition and decomposition of the

[*] Dr. C. Zhao,[+] Dr. Q. Sun, Dr. C. Wang, J. Luo, Dr. X. Lin, Dr. X. Yang, Dr. Y. Zhao, R. Li, Prof. X. Sun
Department of Mechanical and Materials Engineering
University of Western Ontario, London, ON, N6A 5B9 (Canada)
E-mail: xsun@eng.uwo.ca

Dr. Y. Zhu,[+] Prof. M. Gu
Department of Materials Science and Engineering
SUSTech Academy for Advanced Interdisciplinary Studies
Southern University of Science and Technology
Shenzhen, 518055 (China)
E-mail: gum@sustech.edu.cn

Dr. S. Zhao, Dr. L. Zhang, Dr. S. Lu
China Automotive Battery Research Institute Co., Ltd.
Beijing, 100088 (China)

Dr. H. Huang
Glabat Solid-State Battery Inc.
700 Collip Circle, London, ON, N6G 4X8 (Canada)

[+] These authors contributed equally to this work.

Supporting information and the ORCID identification number(s) for the author(s) of this article can be found under:
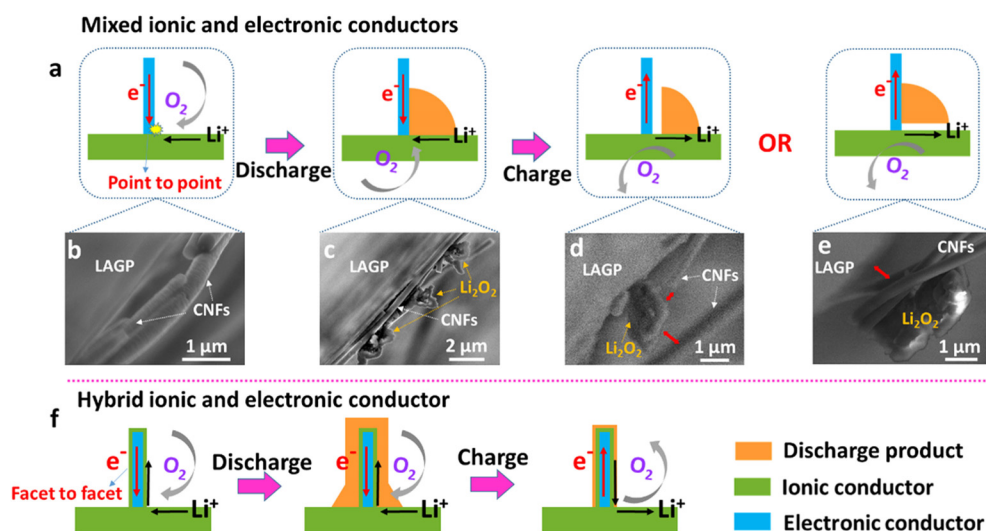https://doi.org/10.1002/anie.202014061.

Figure 1. Illustration and corresponding SEM images to show the discharge-charge process at the interface between ionic and electronic conductors. a) Illustration of the discharge–charge process of Li-O$_2$ batteries with a mixed ionic and electronic conductors electrode. b)–e) SEM images of LAGP|CNFs air electrode at different discharge-charge states of b) before discharging, c) after discharging, d),e) after recharging. f) Illustration of the discharge–charge process of Li-O$_2$ batteries with a hybrid ionic and electronic conductor electrode.

confirm the requirement of both electronic and ionic conduction for the complete formation and decomposition of discharge product. The residue discharge products resulted in low Coulombic efficiency and irreversible consumption of the Li metal anode. Furthermore, the accumulation of dead discharge products continuously occupied the limited space inside the air electrode and caused serious voltage polarization of batteries. Therefore, Li-O$_2$ batteries usually show a poor cycle life. Especially, the solid ionic conductors are not as flexible and accessible to the electronic conductors in the solid-state air cathode as in liquid electrolyte system. Therefore, it is of vital importance to design an air electrode with continuous ions and electrons transport for high-energy-density and long-lifespan solid-state Li-O$_2$ batteries. A hybrid ionic and electronic conducting framework is proposed to achieve uniform ion/electron transport.

We designed and prepared a hybrid ionic and electronic conducting framework with a LiTaO$_3$ coating on NCNT (NCNT@LiTaO$_3$). The hybrid NCNT@LiTaO$_3$ was synthesized by growing NCNT via chemical vapor deposition (CVD) and subsequent coating of LiTaO$_3$ via a sol-gel method.[12] As shown in Figure 2a, the as-prepared NCNT shows a bamboo-like structure with a diameter of 50 nm.
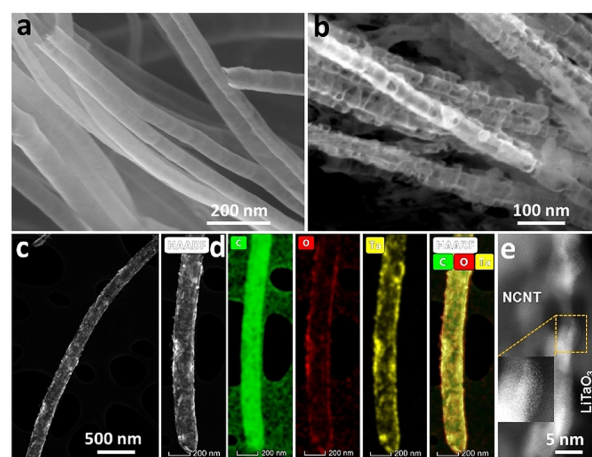
discharge products on the hybrid conductor surface is directly observed.

As shown in Figure 1a and S1, the electrochemical reaction in a typical solid-state Li-O$_2$ battery is a three-phase reaction, which requires electron transfer, ion transport, and O$_2$ supply at the three-phase boundary.[9] If a solid-state air electrode is made of mixed electronic conductor and ionic conductor, electrochemical reaction only occurs at the intersection of the two different conductors with O$_2$ supply due to the poor ionic conductivity (ca. 10^{-19} S cm^{-1}) and electronic conductivity (ca. 10^{-19} S cm^{-1}) of Li$_2$O$_2$.[10] During discharging, once the discharge products cover the intersection of electron/ion transport, further growth of the discharge products is constrained, along with uneven distribution. During charging, the charging process (decomposition of the discharge product) ceases when the discharge products lose contact with either the electronic conductor or the ionic conductor.[11] To verify this postulation, a simple solid-state air electrode was constructed by depositing a very thin layer of carbon nanofibers (CNFs, electron conductor) on the surface of Li$_{1.5}$Al$_{0.5}$Ge$_{1.5}$(PO$_4$)$_3$ (LAGP, ionic conductor) pellet. The cross-section scanning electron microscopy (SEM) image of the as-prepared air electrode is shown in Figure 1b. The loaded CNFs were partially in contact with the LAGP pellet, meeting requirements for initiating the electrochemical reaction of solid-state Li-O$_2$ battery in the presence of electronic and ionic conductors and space for O$_2$ flow. After discharging, the discharge product formed at the intersection between LAGP pellet and CNFs, as shown in Figure 1c. However, after recharging, the discharge product cannot be fully decomposed. The charging process ceased when the discharge product was detached from either the electronic conductor (CNFs, Figure 1d) or the ionic conductor (LAGP pellet, Figure 1e). These observations visually

Figure 2. Morphology characterizations of the hybrid conductor. a),b) SEM images of a) NCNT and b) NCNT@LiTaO$_3$. c) HAADF STEM image of the NCNT@LiTaO$_3$. d) STEM image of NCNT@LiTaO$_3$ and the corresponding elemental mapping. e) High-resolution HAADF STEM image of the NCNT@LiTaO$_3$ and enlarged area of the LiTaO$_3$ layer as inset.

Figure 2b shows an ultrathin and uniform layer of LiTaO$_3$ on the surface of NCNT. The detailed structure of NCNT@Li-TaO$_3$ was further investigated by scanning transmission electron microscopy (STEM). High-angle annular dark-field (HAADF) STEM image of NCNT@LiTaO$_3$ reveals a uniform bright nanotube structure (Figure 2c), in which the brighter contrast at the surface of NCNT is originated from the LiTaO$_3$ layer due to the Z contrast imaging. The uniform distribution of LiTaO$_3$ layer on the surface of NCNT was also confirmed by the energy-dispersive X-ray spectroscopy (EDX) elemental mapping. As shown in Figure 2d, the Ta and O elements are uniformly distributed on the NCNT. In the composite image, the distribution maps of Ta, O, and C elements clearly reveal the presence of a conformal layer of LiTaO$_3$ covering the NCNT. The enlarged HAADF STEM image demonstrates a thickness of approximately 5 nm for the LiTaO$_3$ layer (Figure 2e). The LiTaO$_3$ is considered amorphous without obvious lattice fringe. The ionic conductivity of amorphous LiTaO$_3$ can be as high as 10^{-5} S cm^{-1}.[12]

The composition and chemical states of the hybrid conductor were investigated by X-ray diffraction (XRD) and X-ray photoelectron spectroscopy (XPS). Figure S3 in the Supporting Information shows the XRD patterns of NCNT and NCNT@LiTaO$_3$. The only peak at $2\theta = 26°$ for NCNT@LiTaO$_3$ corresponded to the characteristic peak of NCNT; the absent XRD features of LiTaO$_3$ suggested its amorphous nature, as consistent with the TEM result. The XPS spectra of NCNT@LiTaO$_3$ are shown in the Supporting Information, Figure S4. The XPS survey spectra of NCNT@LiTaO$_3$ indicated an elemental composition of C, N, Li, Ta, and O. The characteristic peaks at 26.4 and 28.3 eV in the Ta 4f XPS spectra were assigned to Ta 4f$_{7/2}$ and Ta 4f$_{5/2}$ of Ta^{5+}, respectively (Supporting Information, Figure S4d). The O 1s peaks centered at 530.8 and 532.8 eV can be ascribed to two types of O species: Ta–O and non-lattice O or absorbed OH, respectively (Supporting Information, Figure S4e). The Ta L-edge X-ray absorption near edge structure (XANES) spectra of Ta metal, commercial LiTaO$_3$, and NCNT@LiTaO$_3$ are shown in the Supporting Information, Figure S5. The NCNT@LiTaO$_3$ features similar characteristic peaks compared to commercial LiTaO$_3$. The XPS and XANES results further confirmed the formation of LiTaO$_3$ on NCNT surface. A hybrid ionic and electronic conductor was successfully prepared. As shown in the Supporting Information, Figure S6, NCNT@LiTaO$_3$ shows a slight decrease in electronic conductivity compared with bare NCNT. But both keep in the same order of magnitude, this is because of the excellent electronic conductivity of NCNT and the uniform and thin LiTaO$_3$ layer.

The electrochemical effects of the hybrid conductor are investigated in solid-state Li-O$_2$ batteries. To make the air electrode, LAGP powders and NCNT@LiTaO$_3$ were mixed, dispersed in alcohol, and dropped on a dense LAGP pallet. After sintering at 700°C for 10 min, the air electrode was obtained. The digital photo and SEM images of the as-prepared air electrode are shown in the Supporting Information, Figure S7. The Li-O$_2$ battery was assembled with a very thin gel polymer electrolyte (GPE) as an interlayer to wet the anode interface and prevent the side reaction between Li

metal and LAGP (Supporting Information, Figures S8 and S9).[13] The electrochemical performance was evaluated by conducting the electrochemical impedance spectroscopy (EIS), cyclic voltammetry (CV), and galvanostatic discharge–charge measurements.

As shown in Figure 3a, the Li-O$_2$ battery with a hybrid conductor exhibits a decreased charge transfer resistance (644 Ω) compared with that with bare NCNT (1248 Ω), indicating faster ionic transport in the NCNT@LiTaO$_3$ electrode.[14] The enhanced electrochemical reaction kinetics of Li-O$_2$ battery with NCNT@LiTaO$_3$ was confirmed by CV test. As shown in Figure 3b, during both discharging (anodic scan) and charging (cathodic scan), the cell with NCNT@Li-TaO$_3$ showed a lower onset overpotential and a higher current density than the NCNT cell. The use of hybrid conductor cathode was demonstrated to significantly improve the kinetics on both ORR and OER processes,[15] thanks to the enhanced effective electrochemical active sites. Consistently, the NCNT@LiTaO$_3$ cell exhibited an obvious decrease in overpotential upon discharging/charging at constant currents (Figure 3c). Compared with that of the NCNT cell, the overpotentials of the NCNT@LiTaO$_3$ cell were significantly lowered by 220 mV and 270 mV during discharge and charge process, respectively, with a limited capacity of 1000 mA h g^{-1} at a current density of 300 mA g^{-1}.

The discharge/charge specific capacities of battery were examined by the galvanostatic discharge-charge test. As shown in Figure 3d, the voltage delay in the initial discharge stage of NCNT@LiTaO$_3$ is attributed to the temporarily lowered dynamics of discharge product nucleation on the surface of NCNT@LiTaO$_3$ caused by the slight decrease of electronic conductivity after coating LiTaO$_3$ on NCNT (Supporting Information, Figure S6). The dynamics balance was achieved over time of discharge. The battery with NCNT@LiTaO$_3$ delivered a high discharge capacity of 12 616 mA h g^{-1} at a current density of 100 mA g^{-1}. By contrast, the battery with bare NCNT exhibited a limited discharge capacity of 7577 mA h g^{-1}. More importantly, the battery with NCNT@LiTaO$_3$ shows a higher Coulombic efficiency of 80.8%, which is more than twice of the NCNT battery (38.6%). At a higher current density of 200 mA g^{-1}, the battery with bare NCNT further dropped to a poor Coulombic efficiency of 11.6%. In sharp contrast, the battery with NCNT@LiTaO$_3$ maintained a high Coulombic efficiency of 82.6% (Figure 3e). The remarkable improvement was attributed to the enhanced Li-ion access on the NCNT@Li-TaO$_3$ cathode by the hybrid conductor framework. The effective electrochemical active area with fast ion- and electron-transfer gave rise to the large specific discharge capacity. Meanwhile, owing to the developed path for ion transport in the NCNT@LiTaO$_3$ air electrode, most of discharge products can be smoothly decomposed, unlike the poor Li$_2$O$_2$ reversibility due to isolation from either ionic or electronic conductors on bare NCNT electrode. The superiority of NCNT@LiTaO$_3$ cathode over NCNT was further demonstrated by the rate performance, as shown in Figure 3f. Upon an increasing current density from 100 to 1000 mA g^{-1}, the specific discharge capacity of the Li-O$_2$ batteries using bare NCNT cathode dramatically dropped by over 35 times to
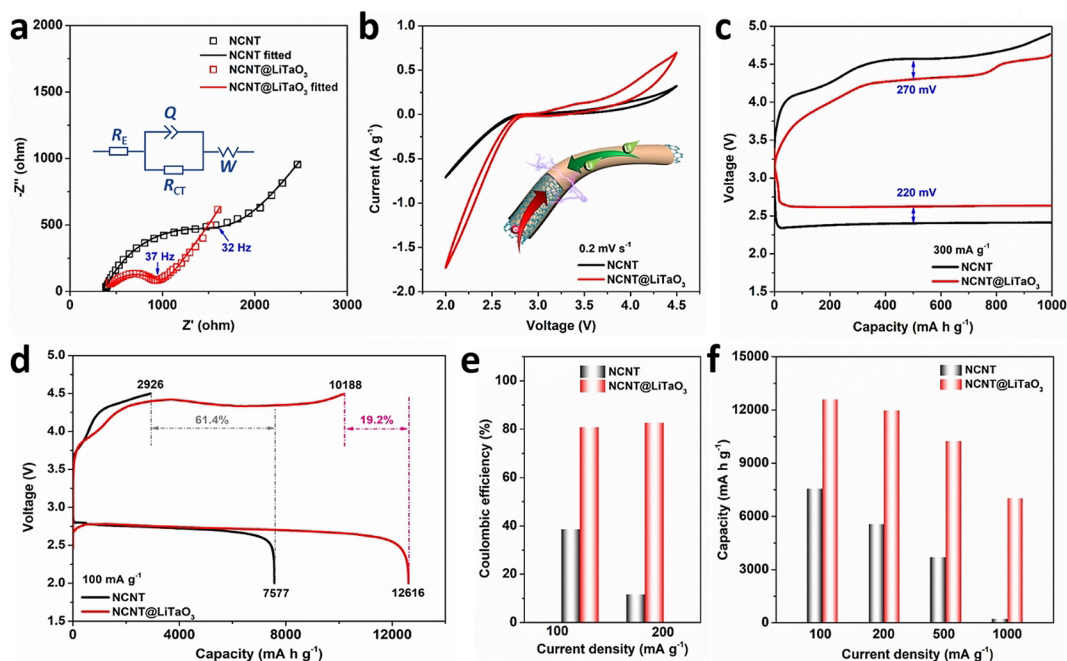
Figure 3. Electrochemical performance of Li-O₂ batteries with a hybrid conductor air electrode. a) Nyquist plots and fitting curves of Li-O₂ batteries with NCNT and NCNT@LiTaO₃; the inset shows the equivalent circuits for fitting. b) CV curves of Li-O₂ batteries with NCNT and NCNT@LiTaO₃; the inset is the illustration of the ion and electron transfer in NCNT@LiTaO₃. c) The initial discharge–charge profiles of Li-O₂ batteries based on NCNT and NCNT@LiTaO₃ at a current density of 300 mA g⁻¹ with a fixed capacity of 1000 mA h g⁻¹. d) The initial discharge-charge profiles of Li-O₂ batteries based on NCNT and NCNT@LiTaO₃ at a current density of 100 mA g⁻¹. e),f) Histograms of e) Coulombic efficiency and f) rate capability of Li-O₂ batteries based on NCNT and NCNT@LiTaO₃.

214 mA h g⁻¹. In contrast, the battery using NCNT@LiTaO₃ delivered a much higher capacity of 7023 mA h g⁻¹ at 1000 mA g⁻¹, which was comparable to the performance of the bare NCNT cell at a 10 times lower current density (100 mA g⁻¹). This further demonstrates the enhanced reaction kinetics of Li-O₂ battery with this hybrid conductor, being in agreement with the EIS and CV results.

The cycling stability of batteries was investigated with a limited capacity of 1000 mA h g⁻¹. As shown in the Supporting Information, Figure S13, the battery with the hybrid conductor exhibits significantly improved cycling performance of 18 cycles compared with 6 cycles of the battery with bare NCNT. Besides, the battery with NCNT@LiTaO₃ maintains an elevated Coulombic efficiency in 17 cycles. In contrast, the Coulombic efficiency of the battery with bare NCNT decreases sharply during cycling. By the 6th cycle, the Coulombic efficiency has dropped to 56.3 %. The EIS results of Li-O₂ batteries after 10 cycles are shown in the Supporting Information, Figure S14. Both Li-O₂ batteries with NCNT and NCNT@LiTaO₃ show increased charge transfer resistance after 10 cycles. In contrast, the battery with NCNT increases sharply, consistent with the bad cycling stability and low Coulombic efficiency. These are because discharge products cannot be efficiently decomposed and gradually accumulate in bare NCNT air electrode, resulting in polarization of the battery. RuO₂ is an effective catalyst for Li-O₂ battery to decrease the overpotential and promote the decomposition of discharge product. To fully demonstrate the effect of the as-prepared hybrid conductor and further enhance the cycle stability of solid-state Li-O₂ battery, the

hybrid of NCNT@LiTaO₃-RuO₂ was prepared by atomic layer deposition RuO₂ particles on the surface of NCNT@LiTaO₃. As shown in the Supporting Information, Figure S13d, the battery with NCNT@LiTaO₃-RuO₂ delivers a lower overpotential compared with that of the batteries with NCNT or NCNT@LiTaO₃ and shows a longer cycle life close to 400 h corresponding to 59 cycles (Supporting Information, Figure S13e).

The deposition and decomposition behaviors of discharge products in the air electrode were investigated by observing the morphology changes of electrode at different discharge-charge states. As shown in Figure 4a, after a shallow discharge, discharge products were uniformly deposited on the
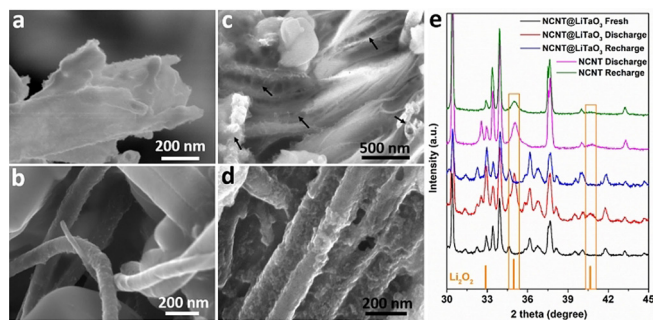

Figure 4. The reversibility of discharge products. a),b) SEM images of a) NCNT@LiTaO₃ and b) NCNT electrodes after partial discharging. c),d) SEM images of the NCNT@LiTaO₃ electrode after c) full discharging and d) recharging. e) XRD patterns of the NCNT@LiTaO₃ and NCNT electrodes at different discharge-charge states.

NCNT@LiTaO$_3$ surface like a coating. On the contrary, the discharge products were only formed at the interface between NCNT and LAGP with large bare uncovered NCNT surface observable due to the lack of fast ion transportation (Figure 4b). After fully discharging, the hybrid conductor of NCNT@LiTaO$_3$ was completely covered by the discharge product, attributed to its fast ion transportation (Figure 4c). After recharging, the discharge product can be decomposed predominantly, exposing the original structure of the air electrode (Figure 4d). In contrast, after fully discharging, the discharge products grew ununiformly in the NCNT air electrode (Supporting Information, Figure S15). After recharging, many remaining discharge product particles were isolated either on NCNT or LAGP. This further highlights the importance of using hybrid conductor for enhancing ion transport kinetics.

To directly probe the dynamic ORR and OER processes with different air cathodes (NCNT@LiTaO$_3$ or NCNT), a solid-state Li-O$_2$ nanobattery was assembled inside an environmental TEM in oxygen gas environment (Figure 5a).[16] The experimental settings enable in situ nanoscale imaging of the electrochemical behavior of hybrid conductor during the discharge and charge process of Li-O$_2$ batteries. NCNT@LiTaO$_3$ was used as both cathode and solid-state electrolyte in the Li-O$_2$ nanobattery, Li metal as the anode. The oxygen environment in the nanobattery was maintained with circa 1 mbar pressure throughout the experiments.

During the discharge and charge process of the solid-state Li-O$_2$ nanobattery, the discharge product shows reversible formation and decomposition on the surface of the NCNT@LiTaO$_3$, and the electrochemical process was in situ monitored by a series of time-resolved TEM images. Figure 5b shows the whole discharge process of in situ solid-state Li-O$_2$ nanobattery with NCNT@LiTaO$_3$. After an incubation time, a thin film of discharge product formed on the surface of NCNT@LiTaO$_3$. Followed by a continuous growth of film, the diameter of the air cathode increases from the initial diameter of about 140 nm to about 200 nm. The corresponding selected area electron diffraction pattern (Supporting Information, Figure S17) confirms the formation of Li$_2$O$_2$ discharge products (PDF: 09-0355). Upon recharging, the deposited film can be reversibly decomposed, and the diameter of the composition recovers to the initial value (Figure 5c). The corresponding dynamic movie for Figure 5b,c can be found in the supplementary materials (Supporting Information, Movie S1). Furthermore, we also can observe that the discharge product can smoothly form and grow inside the tube of NCNT owing to the existence of pore and ionic conductor on the surface of NCNT (Supporting Information, Figures S18 and S19, Movie S2). By contrast, the discharge product formed in the in situ solid-state Li-O$_2$ nanobattery with bare NCNT shows a particle-shaped morphology in agreement with the results reported previously (Figure 5d).[17] As shown in Figure 5e, a discharge product sphere formed and grew at the contact point between Li metal and NCNT during discharge. Upon recharge, the discharge product particle shrank, but it was not decomposed completely. There were residue particles remaining even after a long operation time because separation from either ionic or electronic conductor ceased the charging of the particles
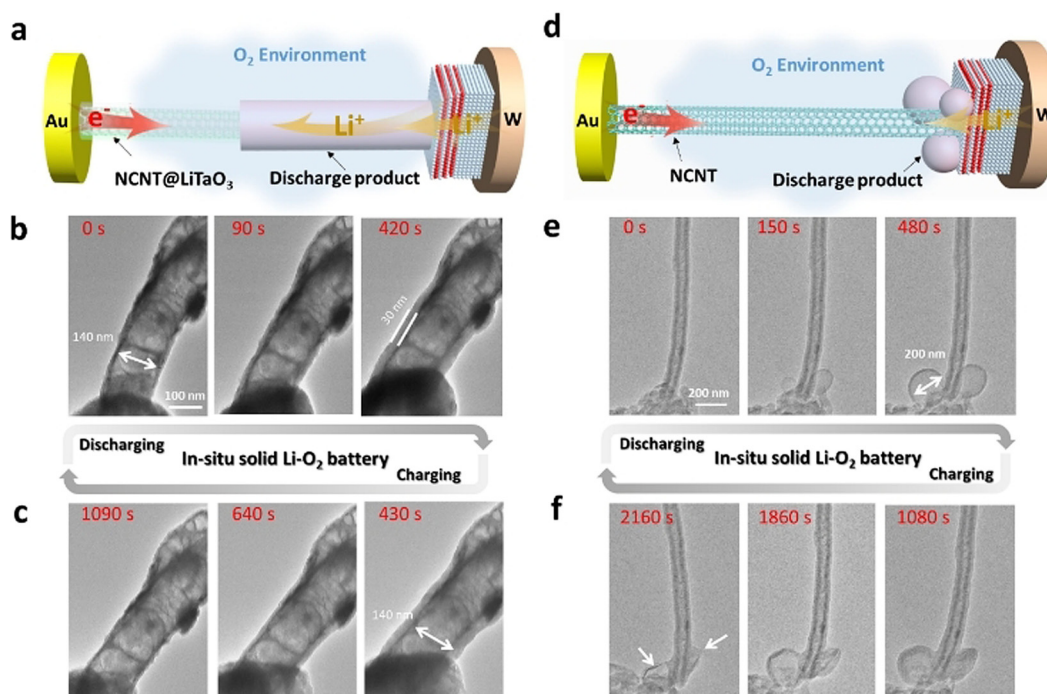

Figure 5. In situ observation of the morphological evolution of the discharge product. a) Illustration of the configuration of the in situ solid-state Li-O$_2$ nanobattery with NCNT@LiTaO$_3$ in an environmental TEM chamber. b),c) In situ TEM images of time-resolved b) discharge and c) charge processes with NCNT@LiTaO$_3$ hybrid ionic and electronic conductor. d) Illustration of the configuration of the in situ solid-state Li-O$_2$ nanobattery with NCNT in an environmental TEM chamber. e),f) In situ TEM images of time-resolved e) discharge and f) charge processes with NCNT.

(Figure 5 f). The corresponding dynamic movie can be found in the Supporting Information, Movie S3. Based on these results, the coating of LiTaO$_3$ was proven to act as an electrolyte for Li-ion transport, and the hybrid conductor can be used as a host for the deposition and decomposition of discharge product.

In summary, we have successfully designed and prepared a hybrid ionic and electronic conductor for air electrode of Li-O$_2$ battery to enhance its electrochemical reaction kinetics by achieving fast ionic transport in the air electrode. As a result, the interfacial resistance is significantly decreased, and reaction kinetics is much enhanced. Real-time visualization of the charge and discharge processes are obtained using in situ environmental TEM. Besides, the discharge product can smoothly form and decompose on the surface of the hybrid conductor, resulting in a dramatically enhanced Coulombic efficiency from 38.6% to 80.8%. It is expected that the present study can shed light on the improvement of air electrodes and development for solid-state Li-O$_2$ batteries.

Conflict of interest

The authors declare no conflict of interest.

[1] a) C. Zhao, C. Yu, M. N. Banis, Q. Sun, M. Zhang, X. Li, Y. Liu, Y. Zhao, H. Huang, S. Li, X. Han, B. Xiao, Z. Song, R. Li, J. Qiu, X. Sun, *Nano Energy* **2017**, *34*, 399–407; b) J. Lu, L. Li, J.-B. Park, Y.-K. Sun, F. Wu, K. Amine, *Chem. Rev.* **2014**, *114*, 5611–5640; c) Z. Guo, C. Li, J. Liu, Y. Wang, Y. Xia, *Angew. Chem. Int. Ed.* **2017**, *56*, 7505–7509; *Angew. Chem.* **2017**, *129*, 7613–7617; d) Q.-C. Liu, T. Liu, D.-P. Liu, Z.-J. Li, X.-B. Zhang, Y. Zhang, *Adv. Mater.* **2016**, *28*, 8413–8418; e) K. Liao, S. Wu, X. Mu, Q. Lu, M. Han, P. He, Z. Shao, H. Zhou, *Adv. Mater.* **2018**, *30*, 1705711.

[2] a) X. Zou, Q. Lu, Y. Zhong, K. Liao, W. Zhou, Z. Shao, *Small* **2018**, *14*, 1801798; b) D. Lin, Y. Liu, Y. Cui, *Nat. Nanotechnol.* **2017**, *12*, 194; c) X.-B. Cheng, R. Zhang, C.-Z. Zhao, Q. Zhang, *Chem. Rev.* **2017**, *117*, 10403–10473; d) Z. Huang, J. Ren, W. Zhang, M. Xie, Y. Li, D. Sun, Y. Shen, Y. Huang, *Adv. Mater.* **2018**, *30*, 1803270; e) Y. Li, X. Wang, S. Dong, X. Chen, G. Cui, *Adv. Energy Mater.* **2016**, *6*, 1600751.

[3] a) C. Zhao, J. Liang, Q. Sun, J. Luo, Y. Liu, X. Lin, Y. Zhao, H. Yadegari, M. N. Banis, R. Li, H. Huang, L. Zhang, R. Yang, S. Lu, X. Sun, *Small Methods* **2019**, *3*, 1800437; b) X. B. Zhu, T. S. Zhao, Z. H. Wei, P. Tan, G. Zhao, *Energy Environ. Sci.* **2015**, *8*, 2782–2790; c) X. B. Zhu, T. S. Zhao, Z. H. Wei, P. Tan, L. An, *Energy Environ. Sci.* **2015**, *8*, 3745–3754; d) J. Yi, S. Guo, P. He, H. Zhou, *Energy Environ. Sci.* **2017**, *10*, 860–884; e) M. Balaish, E. Peled, D. Golodnitsky, Y. Ein-Eli, *Angew. Chem. Int. Ed.* **2015**, *54*, 436–440; *Angew. Chem.* **2015**, *127*, 446–450.

[4] a) Y. Liu, B. Li, Z. Cheng, C. Li, X. Zhang, S. Guo, P. He, H. Zhou, *J. Power Sources* **2018**, *395*, 439–443; b) Y. Liu, P. He, H. Zhou, *Adv. Energy Mater.* **2018**, *8*, 1701602; c) X. Wang, D. Zhu, M. Song, S. Cai, L. Zhang, Y. Chen, *ACS Appl. Mater. Interfaces* **2014**, *6*, 11204–11210.

[5] a) A. Manthiram, X. Yu, S. Wang, *Nat. Rev. Mater.* **2017**, *2*, 16103; b) B. Wu, S. Wang, W. J. Evans IV, D. Z. Deng, J. Yang, J. Xiao, *J. Mater. Chem. A* **2016**, *4*, 15266–15280; c) L. Xu, S. Tang, Y. Cheng, K. Wang, J. Liang, C. Liu, Y.-C. Cao, F. Wei, L. Mai, *Joule* **2018**, *2*, 1991–2015.

[6] a) W. Zhao, J. Yi, P. He, H. Zhou, *Electrochem. Energy Rev.* **2019**, *2*, 574–605; b) M. D. Tikekar, S. Choudhury, Z. Tu, L. A. Archer, *Nat. Energy* **2016**, *1*, 16114; c) X. Yu, A. Manthiram, *Energy Environ. Sci.* **2018**, *11*, 527–543; d) X. Yu, A. Manthiram, *Acc. Chem. Res.* **2017**, *50*, 2653–2660.

[7] a) J. Sun, N. Zhao, Y. Li, X. Guo, X. Feng, X. Liu, Z. Liu, G. Cui, H. Zheng, L. Gu, H. Li, *Sci. Rep.* **2017**, *7*, 41217; b) G. A. Elia, J. Hassoun, *Sci. Rep.* **2015**, *5*, 12307; c) J. Yi, H. Zhou, *ChemSusChem* **2016**, *9*, 2391–2396.

[8] Y. Liu, J. Yi, Y. Qiao, D. Wang, P. He, Q. Li, S. Wu, H. Zhou, *Energy Storage Mater.* **2018**, *11*, 170–175.

[9] N. Bonnet-Mercier, R. A. Wong, M. L. Thomas, A. Dutta, K. Yamanaka, C. Yogi, T. Ohta, H. R. Byon, *Sci. Rep.* **2014**, *4*, 7127.

[10] X. Zhu, T. Zhao, P. Tan, Z. Wei, M. Wu, *Nano Energy* **2016**, *26*, 565–576.

[11] L. Zhong, R. R. Mitchell, Y. Liu, B. M. Gallant, C. V. Thompson, J. Y. Huang, S. X. Mao, Y. Shao-Horn, *Nano Lett.* **2013**, *13*, 2209–2214.

[12] W. Zhang, D. A. Weber, H. Weigand, T. Arlt, I. Manke, D. Schröder, R. Koerver, T. Leichtweiss, P. Hartmann, W. G. Zeier, J. Janek, *ACS Appl. Mater. Interfaces* **2017**, *9*, 17835–17845.

[13] a) H. Kitaura, H. Zhou, *Sci. Rep.* **2015**, *5*, 13271; b) Y. Zhu, X. He, Y. Mo, *ACS Appl. Mater. Interfaces* **2015**, *7*, 23685–23693.

[14] a) S. Xu, D. W. McOwen, C. Wang, L. Zhang, W. Luo, C. Chen, Y. Li, Y. Gong, J. Dai, Y. Kuang, C. Yang, T. R. Hamann, E. D. Wachsman, L. Hu, *Nano Lett.* **2018**, *18*, 3926–3933; b) C. Yang, H. Xie, W. Ping, K. Fu, B. Liu, J. Rao, J. Dai, C. Wang, G. Pastel, L. Hu, *Adv. Mater.* **2019**, *31*, 1804815; c) Z. Li, W.-X. Sha, X. Guo, *ACS Appl. Mater. Interfaces* **2019**, *11*, 26920–26927.

[15] C. Zhao, C. Yu, S. Liu, J. Yang, X. Fan, H. Huang, J. Qiu, *Adv. Funct. Mater.* **2015**, *25*, 6913–6920.

[16] a) W.-J. Kwak, L. Luo, H.-G. Jung, C. Wang, Y.-K. Sun, *ACS Energy Lett.* **2018**, *3*, 393–399; b) Q. Liu, T. Yang, C. Du, Y. Tang, Y. Sun, P. Jia, J. Chen, H. Ye, T. Shen, Q. Peng, L. Zhang, J. Huang, *Nano Lett.* **2018**, *18*, 3723–3730; c) X. Wu, S. Li, B. Yang, C. Wang, *Electrochem. Energy Rev.* **2019**, *2*, 467–491.

[17] L. Luo, B. Liu, S. Song, W. Xu, J.-G. Zhang, C. Wang, *Nat. Nanotechnol.* **2017**, *12*, 535.